



FIRST YEAR INTERIM REPORT

# **The Motional Stark Effect Diagnostic:**

Measurements on MAST-U

Sam Gibson

supervised by  
Prof. R. M. Sharples

February 25, 2019

# Contents

<b>1</b>	<b>Introduction</b>	<b>1</b>
1.1	Why do we need fusion? . . . . .	1
1.2	Fusion Energy . . . . .	2
1.3	Tokamaks . . . . .	4
1.3.1	Plasma Confinement . . . . .	4
1.3.2	The Mega Amp Spherical Tokamak (MAST) . . . . .	6
1.3.3	MAST Upgrade . . . . .	6
1.4	Motional Stark Effect Diagnostic on MAST-U . . . . .	8
<b>2</b>	<b>MSE System on MAST-U</b>	<b>9</b>
2.1	MSE Theory . . . . .	9
2.1.1	Motional Stark Effect . . . . .	9
2.2	Overview of MSE Diagnostic . . . . .	9
2.3	Stokes Polarimetry . . . . .	11
2.3.1	Stokes Vectors . . . . .	11
2.3.2	Dual Photoelastic Modulator System . . . . .	11
2.4	MSE Measurements . . . . .	12
2.5	EFIT++ Equilibrium Reconstruction . . . . .	12
2.5.1	Outputs from EFIT++ . . . . .	13
2.5.2	Magnetic Field Reconstruction . . . . .	13
2.6	Current and Future Work . . . . .	16
	<b>Bibliography</b>	<b>17</b>

# Chapter 1

## Introduction

### 1.1 Why do we need fusion?

World population is expected to reach 8 billion by around 2030s and global energy consumption will rise accordingly. Energy demand is currently met with fossil fuels such as crude oil and natural gas, though reserves are in decline. Fossil fuels increase atmospheric concentration of greenhouse gases and facilitate climate change. In order to meet global energy demand in a sustainable manner, the future energy mix needs to be a variety of low carbon energy sources. The success of renewables such as solar and wind power depend heavily on the environmental conditions, meaning another form of carbon free energy is needed to meet the base load. Nuclear fission makes a small contribution towards meeting our energy demands, but most of these fission power plants are largely out of date, inefficiently use fuel and produce large amounts of long lived nuclear waste. Newer fission power plants are designed to combat these issues, but the nuclear energy industry still faces criticism from the general public due to safety concerns.

Nuclear fusion can provide low carbon energy safely. There is no possibility of a runaway reaction such as those seen in fission plants. The materials used for nuclear fusion include two isotopes of hydrogen: Deuterium, which is abundant in sea water, and tritium, a radioactive isotope with a half life of around 12.3yrs. Tritium is not a naturally occurring isotope of hydrogen and must be bred from lithium. Due to the plentiful abundance of deuterium and lithium, nuclear fusion could provide us with energy indefinitely.

However, we may not see electricity on the national grid produced by a nuclear fusion plant until the latter half of this century. Current fusion reactors such as the Joint European Torus (JET) in the UK has reached ratios of fusion power to input power of  $\approx 62\%$ . JET has paved the way for the new generation of fusion reactors such as ITER, which should achieve the required milestones so that we can build successful and economic fusion power plants. ITER will be the first reactor that demonstrates steady state operation with an output power of 500MW for an input of 50MW. It will also allow us to test technology required for power plants like breeder blankets that harness neutrons to breed extra tri-

tium. These reactors prepare us for designing and constructing the first demonstration power plant, DEMO, which will hopefully supply electricity to the grid. Smaller devices such as the Mega Amp Spherical Tokamak (MAST) also in the UK have a key role in this road-map to fusion, exploring a variety of reactor configurations to optimize operational parameters. MAST tackles many still unsolved physics problems which could hinder the progress of ITER.

The majority of time spent on this PhD project will be using a diagnostic on MAST, known as the Motional Stark Effect (MSE) diagnostic. Plasma diagnostics are vital for information on key plasma parameters. Beam emission diagnostics rely on neutral atoms injected into the plasma via a neutral beam heating system, used for current drive and charge exchange which sustains plasma heating. Passive spectroscopy diagnostics such as MSE observe emission from the plasma to determine local plasma properties, which are important for plasma stability and control.

As part of the Center for Doctoral Training (CDT), the first six months of the PhD are spent at the York Plasma Institute undertaking graduate training in the form of an introduction to fusion and plasma physics. I was then relocated to the Culham Center for Fusion Energy (CCFE) to begin research and work on the MSE diagnostic from the beginning of April 2017. The bulk of this report will be an overview of fusion and plasma physics to demonstrate the knowledge gained through the taught courses at York. Some preliminary work is included towards the end of this report, which will be built upon in the coming months.

## 1.2 Fusion Energy

Light elements, such as isotopes of hydrogen, fuse together under high temperature and pressure conditions to release energy and form heavier elements. The dominant fusion mechanism in the Sun occurs on an extremely slow timescale, on the order of a million years. Two protons fuse into a deuteron ( ${}^2\text{H}$ ) and release a positron. A third proton then fuses with the deuteron to produce a light isotope of helium  ${}^3\text{He}$ . The final step includes fusing two light helium nuclei to create  ${}^4\text{He}$  and two protons, which further the chain reaction. A practical fusion system reliant on proton-proton fusion is unfeasible; the cross section of the reaction is, albeit acceptable on the scale of the dimensions of the Sun, too small to generate enough power to sustain a fusion reactor on Earth. The cross section of the reaction characterizes the likelihood of collisions, given the energy of the reactants [1]. The fusion reaction which most commonly used is between deuterium ( ${}^2_1\text{D}$ ) and tritium ( ${}^3_1\text{T}$ ),



The probability of fusion occurring is low at small energies as the two fusing nuclei must

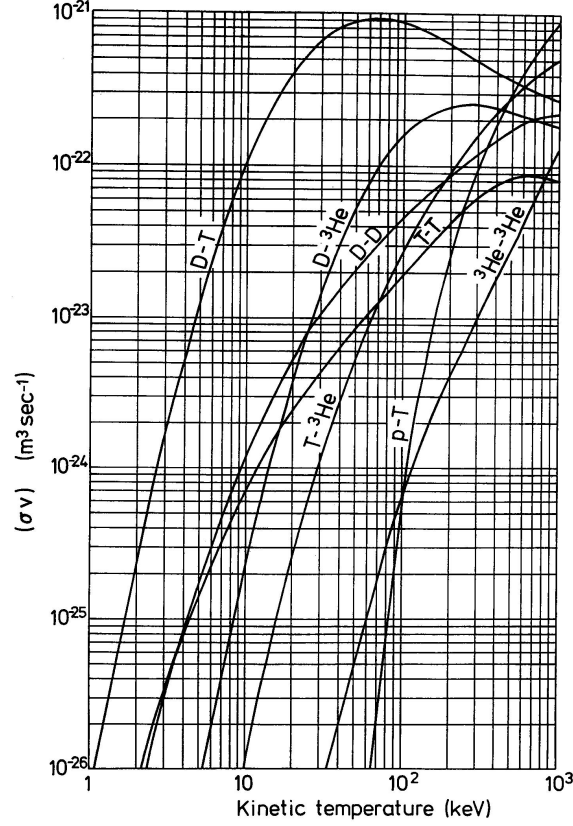


Figure 1.1: Reactivity of various fusion reactions as a function of energy [3]. DT fusion has the highest reactivity at physically feasible temperatures ( $\approx 10\text{-}20\text{keV}$ ).  ${}^3\text{He-}{}^3\text{He}$  fusion is aneutronic which improves the lifetime of the reactor, but the temperature required to reach peak reactivity is too high.

overcome the repulsive Coulomb potential. However, there is a small but finite chance for nuclei with energies smaller than the Coulomb barrier to fuse due to quantum tunneling. Maximizing fusion energy output is not as simple as just maximizing the fusion cross section alone. We require a Maxwellian distribution with a width determined by the thermal velocity of the particles within the plasma to conserve their kinetic energy,

$$f_M(\mathbf{r}, \mathbf{v}) = \frac{n(\mathbf{r})}{[2\pi v_{th}^2(\mathbf{r})]^{\frac{3}{2}}} \exp\left(\frac{-v^2}{2v_{th}^2}\right) \quad (1.2.2)$$

The reactivity  $\langle \sigma v \rangle$  is defined by taking the integral of the Maxwellian distribution over all velocity space, which is a function of the plasma density and temperature. We ideally want a high reactivity at feasible kinetic temperatures, which is one of the main benefits of DT fusion.

The confinement time of the plasma  $\tau_E$  is given as the ratio of the total energy stored in the plasma  $U$  to the energy loss  $E_L$ ,  $\tau_E = \frac{U}{E_L}$ . Confinement time is dependent on temperature; higher temperatures increase reactivity hence more fusion reactions will occur, but this results in poor confinement time due to energy loss and a decrease in fuel density. Energy

is mainly lost from the system as particle confinement is not perfect. Particles leave the plasma due to turbulence and drifts, which can be slightly counteracted by certain magnetic configurations. Energy is also lost in the form of X-ray radiation from impurities, which scales as  $Z^2$ . This becomes an issue in fusion reactors where sections of the tokamak are made from high  $Z$  materials like tungsten. A steady state plasma would require these losses to be balanced by heating power, which could either be externally applied or from the plasma itself [2]. In tokamaks  $^4\text{He}$ , or alpha particles, can provide the necessary heating granted that the temperature of the plasma is high enough for significant fusion yield. This leads to the Lawson criteria, or triple product, which maximizes confinement time  $\tau_E$ , the temperature of the distribution  $T$  and the particle density  $n$ ,

$$nT\tau_E = \frac{12}{\langle \sigma V \rangle} \frac{T^2}{E_\alpha} \quad (1.2.3)$$

which is approximately equal to  $3 \times 10^{21} \text{ m}^{-3} \text{ keVs}$  for a tokamak reactor operating in the range of 10-20keV, confining  $10^{20} \text{ m}^3$  for on the order of a few seconds. The  $Q$  factor is an important performance parameter to measure the efficiency of a fusion reactor, which is the ratio of the fusion power output to the external heating required,

$$Q = \frac{P_{out}}{P_{ext}} \quad (1.2.4)$$

For a reactor to break even, this requires  $Q=1$ . In the case where the triple product requirement is met, then external heating power can be turned off and fusion is sustained through internal alpha heating, corresponding to the limit  $Q \rightarrow \infty$ .

## 1.3 Tokamaks

### 1.3.1 Plasma Confinement

How is it possible to confine a plasma? The most successful attempts so far use magnetic fields in a device known as a tokamak; a large cylindrical solenoid shaped into a torus to improve plasma confinement. The tokamak co-ordinate system  $(R, Z, \phi)$  is shown in Fig. 1.2. The major radius  $R_0$  is defined from the toroidal axis to the center of the plasma. The minor radius  $r$  is defined from the magnetic axis. The radius of the plasma is denoted as  $a$ , from which we can define an aspect ratio  $R_0/a$ . The toroidal aspect ratio gives a measure of "fatness" of the torus.

Toroidal field coils are shown in Fig.1.4, which wrap around the torus and produce the toroidal magnetic field  $B_\phi$ . A toroidal plasma current is generated by ramping current through the central solenoid located on the toroidal axis, equivalent to a transformer. The change in flux induces a toroidal electric field that drives a plasma current due to opposing toroidal flows of ions and electrons. This plasma current further generates a poloidal magnetic field  $B_\theta$ . Finally, further poloidal field coils are added for plasma shaping and control.  $B_\theta$  and  $B_\phi$  combine resulting in helical magnetic field lines, shown in

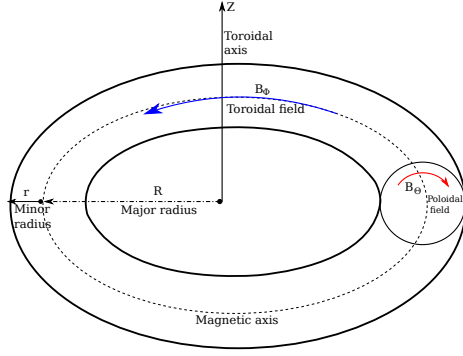


Figure 1.2: Tokamak reactor showing machine co-ordinates  $(R, Z, \phi)$  with directions of the poloidal and toroidal magnetic fields.

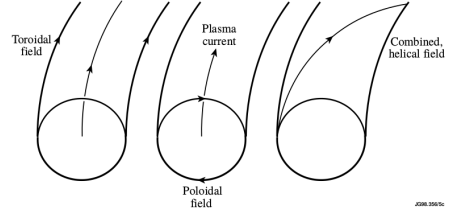


Figure 1.3: Representation of helical magnetic field structure from combining  $B_\theta$  and  $B_\phi$  [1].

Fig. 1.3.1. Particles are confined along these field lines due to the Lorentz force. The magnitude of the toroidal and poloidal components of the magnetic field vary depending on position within the tokamak. The magnetic field lines do not cross, so each magnetic flux surface  $\psi$  has a particular ratio of poloidal to toroidal field, which is known as the safety factor  $q$ . The value of  $q$  is a function of major radius  $R$ , also known as a  $q$  profile.

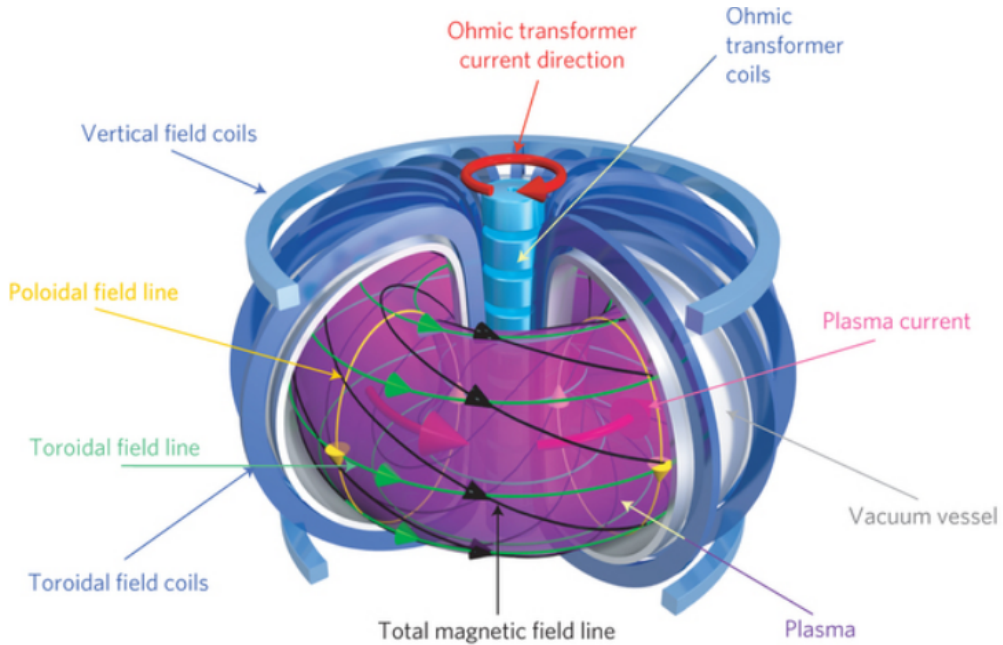


Figure 1.4: Example of a spherical tokamak with field coils and the respective magnetic fields [4].

### 1.3.2 The Mega Amp Spherical Tokamak (MAST)

MAST is a tight aspect ratio ( $R_0/a = 1.5$ ) spherical tokamak (ST) which can achieve plasma currents of up to 2.0 MA. They tend to have smaller magnetic fields than large aspect ratio tokamaks. STs confine plasma more efficiently as less B field is required to confine the same plasma density; The ratio of the plasma pressure to the magnetic field pressure, known as  $\beta$ , is higher. High  $\beta$  values improve the economic feasibility of a fusion reactor. Another benefit includes a much higher value for the safety factor  $q$ . Particles move along magnetic field lines within the tokamak and spend significantly longer on the inboard side than the outboard, which reduces 'bad' curvature within the plasma.

The magnetic field lines on MAST are arranged so that escaping plasma is exhausted into a separate area of the tokamak, where it is then neutralised. This area is known as a divertor and they are now prevalent on the majority of large scale tokamaks around the world. The purpose of the divertor is to:

- Impurity control via transport in the SOL, as they can lower the plasma temperature in the core.
- Exhaust power from the plasma during disruptions.
- Reduce helium ash to avoid fuel dilution.

The divertor has more advantages such as making higher efficiency confinement modes (H Mode) easier to reach. Different divertor geometries are shown in Fig.1.5.

### 1.3.3 MAST Upgrade

An upgrade to MAST (MAST-U) is almost completed, with first physics set for early 2018. Divertor geometry and exhaust physics are key research areas and are important to the success of ITER and fusion power plant designs. The new MAST-U divertor is highly configurable for a range of working scenarios; from the original inner leg divertor where plasma forms an X point close to the plasma itself, up to the Super-X configuration which stretches out the 'plasma leg' to  $R=1.5\text{m}$ . Particles now have to travel significantly further on their spiral trajectories from the core to the divertor whilst emitting radiation, meaning by the time they hit divertor tiles the power flux per unit area will be significantly smaller. Different divertor configurations means MAST-U could achieve higher values of  $\beta$  and improved impurity control.

Another key mission for MAST-U is understanding plasma stability and performance limiting Edge Localised Modes (ELMs). ELMs reduce the achievable pulse length, therefore they need to be mitigated. This can be achieved through accurate edge measurements of the current density  $j_\phi$  and  $q$  profile. Instabilities within the plasma arise when  $q$  is irrational, which motivates the requirement for real time control and tailoring of  $q$  profiles.



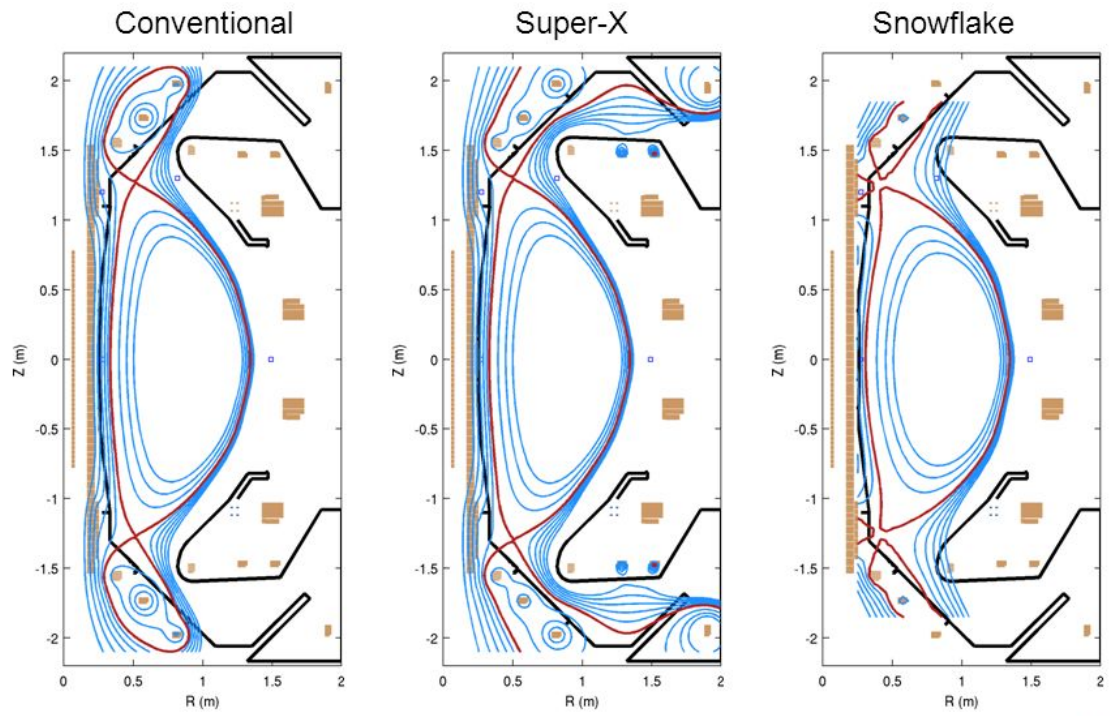


Figure 1.5: An overview of divertor geometries for MAST-U. [5]. The super-X divertor increases the connection length of the particles, providing a lower heat flux per unit area. The snowflake divertor offers the ability to deposit heat flux between several divertor channels.

Combining measurements from diagnostics with codes that analyse plasma stability can provide greater understanding of the conditions for stability and reconstruct the magnetic field within the plasma.

## 1.4 Motional Stark Effect Diagnostic on MAST-U

The motional Stark effect (MSE) diagnostic is a passive beam spectroscopy diagnostic. Fast particles from the neutral beam heating system move across a magnetic field. They experience a Lorentz electric field  $\mathbf{E} = \mathbf{V} \times \mathbf{B}$  in their rest frame. The Stark effect causes wavelength splitting of the Balmer series and light emission is polarized with respect to the radial electric field in the plasma  $E_R$ , depending on the change in magnetic quantum number between states. The Lorentz  $\mathbf{E}$  field and  $\mathbf{B}$  field are orthogonal. The MSE diagnostic measures the polarization angle of light emission; a variation in polarization angle corresponds to a variation in magnetic pitch angle  $\gamma_m$ . This diagnostic can give insight into the current density derived from measurements of  $\gamma_m$  and also the  $q$  profile across a plasma.

## Chapter 2

# MSE System on MAST-U

### 2.1 MSE Theory

#### 2.1.1 Motional Stark Effect

The MSE diagnostic observes polarized light emission from neutral hydrogen atoms, which experience a Lorentz  $\mathbf{E}$  field in their rest frame as they move across a magnetic field. The first order perturbation of the energy eigenstates dominates, known as the linear Stark effect because the change in energy is proportional to the  $E$  field (around 100kV/cm.) An explicit solution to the Schrodinger equation for a hydrogen atom subjected to an external electric field can be determined in parabolic coordinates. The Stark eigenstates are described by,

$$n_1 + n_2 = n - |m| - 1 \quad (2.1.1)$$

where  $n_1$  and  $n_2$  are the electric quantum numbers and  $m$  is the magnetic quantum number [6]. Allowed electric dipole transitions include those where the change in magnetic quantum number  $\Delta m = 0, \pm 1$ .  $\Delta m = 0$  corresponds to light emission polarized parallel to the  $E$  field, known as linear  $\pi$  emission and  $\Delta m = \pm 1$  corresponds to circularly polarized  $\sigma$  emission. If light emission is observed along the axis of  $\mathbf{E}$ , then only  $\sigma$  emission is viewed. The MSE system focuses on transitions from  $n=3$  to  $n=2$  Balmer- $\alpha$  ( $H_\alpha = 656.3$  nm) as this is the most intense line within the visible, so conventional optics can be implemented [7]. The allowed electric dipole transitions for  $H\alpha$  are shown in Fig.2.1

### 2.2 Overview of MSE Diagnostic

A diagram of the MSE diagnostic is shown in Fig. 2.2. Light emission from the plasma passes through the dual photoelastic modulator (PEM) system, then through a linear polarizer. The PEM system allows polarization information to be stored as an intensity modulation, as the optical fibers do not preserve light polarization. The wavelength of light emission from the neutral beam varies across each viewing chord due to Doppler shift. The energy of the neutral beam then determines the central wavelength of the narrowband

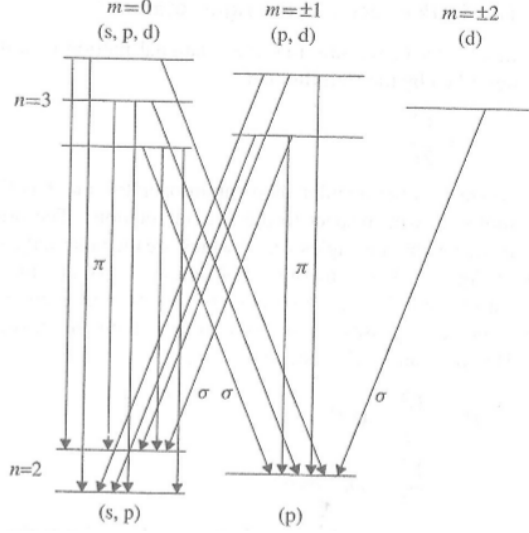


Figure 2.1: Electric dipole transitions between  $n=3$  and  $n=2$  states of hydrogen [8].

filter for each channel. Narrow bandpass filters with a bandwidth of 0.12nm FWHM select the correct doppler shifted  $\sigma$  light component. Around 35 channels out of 42 are active per shot due to beam energy variation of around 10keV. The avalanche photodiodes (APD) collect and relay the signal to a set of lock in amplifiers.

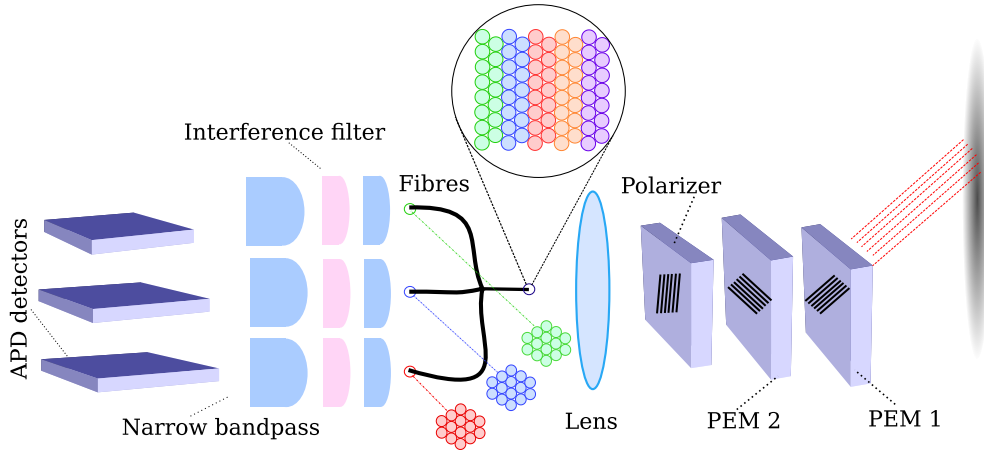


Figure 2.2: Optical setup of the MSE system. Optical fibers show hexagonal packing arrangement to minimize broadening of the filter bandshape.

## 2.3 Stokes Polarimetry

### 2.3.1 Stokes Vectors

The polarization state of light emission from the plasma is described by Stokes' parameters. These are a set of four time averaged components of the wave and give the fraction of light which is linearly or circularly polarized.

$$S = \begin{bmatrix} I \\ Q \\ U \\ V \end{bmatrix} = \begin{bmatrix} I \\ IP_L \cos(2\gamma) \\ IP_L \sin(2\gamma) \\ IP_C \end{bmatrix} \quad (2.3.2)$$

where  $P_L$  is the linear polarization fraction,  $P_C$  is the circular polarization fraction,  $\gamma$  is the linear polarization angle with respect to the horizontal axis and  $I$  is the light intensity. The polarization fractions sum in quadrature  $P = \sqrt{P_C^2 + P_L^2}$ , as the intensity  $I$  is proportional to the square of the electric field. The change in polarization state of the light due to passing through optical elements in the system can be represented by Muller matrices.

### 2.3.2 Dual Photoelastic Modulator System

The main aspect of the MSE diagnostic are the photoelastic modulators (PEMs). PEMs have the ability to measure fine changes in polarization measurements. A piezoelectric transducer is tuned to the resonant frequency of a transparent optical element. A time dependent stress is induced in the optical element by passing a current through the transducer. This causes uniaxial birefringence where the refractive index  $n$  varies along one axis of the PEM. As polarized light travels through the PEMs, the photoelastic effect causes a time varying phase retardance between the parallel and perpendicular components of the light. These waves are combined with a polarizer orientated at  $22.5^\circ$ . The total light intensity signal is now dependent on the retardance set by the PEMs. The modulation amplitudes can be expanded into harmonics with solutions in the form of  $n$ th order Bessel functions  $J_z(A)$ . Hence we can determine polarization angle using the ratio of the amplitudes of these harmonics [9], [10], [11].

In the MSE system, a dual PEM polarimeter is used, where two PEMs are mounted with axis  $45^\circ$  apart so that the ratio of the modulation amplitudes retrieve the polarization angle. Retardances are given by  $A_1 = |A_1| \cos(\omega_1 t)$  for the first PEM and  $A_2 = |A_2| \cos(\omega_2 t)$  for the second. The amplitude of retardance is set at  $|A_1| = |A_2| = \pi$  or  $\pm$  half a wave and the driving frequencies are set at  $\omega_1 = 2\pi 20\text{kHz}$  and  $\omega_2 = 2\pi 23\text{kHz}$ .

## 2.4 MSE Measurements

We calculate the pitch angle, ie. the ratio of the toroidal to the poloidal magnetic field using the polarization angle,

$$\tan(\gamma) = \frac{-\cos(\beta)B_\theta - (E_r/v)\cos(\alpha + \beta)}{\sin(\alpha)B_\phi} \quad (2.4.3)$$

where  $E_r$  is the radial electric field,  $v$  is the beam velocity,  $B_\theta$  is the poloidal magnetic field,  $B_\phi$  the toroidal magnetic field and  $\alpha$  and  $\beta$  are the angles between the beam and toroidal unit vector and between the beam and line of sight respectively.

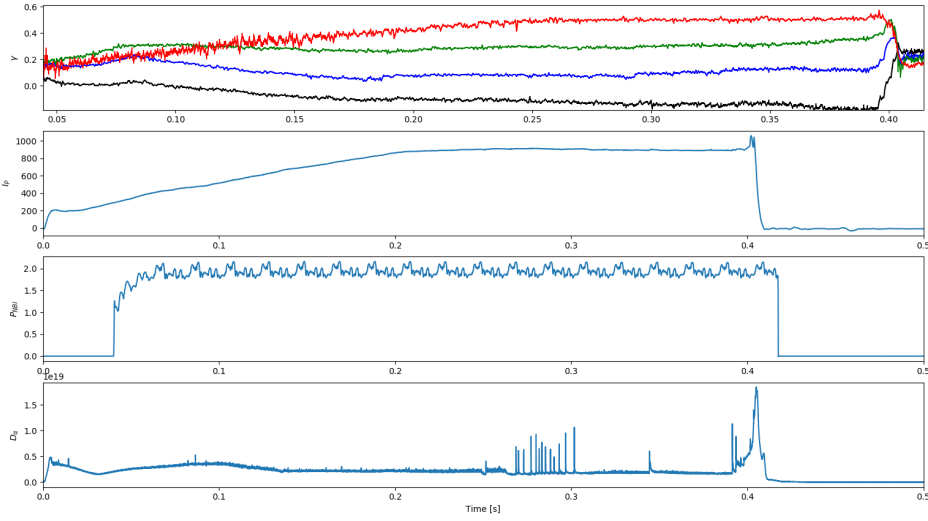


Figure 2.3: **Top to bottom:** Polarization angle  $\gamma$  from four viewing chords placed radially across the plasma. The black line is furthest to the edge and the red line towards plasma core.) Plasma current  $I_P$ . Neutral beam heating power  $P_{NBI}$ . Alpha particle light emission from the plasma.

Fig.2.3 shows a typical output from MSE of the polarisation angle measured across a shot. Slight variations in the neutral beam power can cause changes in polarization angle. From the top plot in Fig. 2.3, we can see that polarization angle increases towards the plasma core. This is as expected, closer to the plasma core the toroidal field dominates over the poloidal field, giving a large variation in pitch angle. Plotting the  $D_\alpha$  emission shows the ELM frequency, which is much faster in high confinement modes.

## 2.5 EFIT++ Equilibrium Reconstruction

The measurements MSE make are crucial for constraining plasma equilibrium codes. Reconstruction codes seek to reconstruct the shape and parameters present in a plasma for

a particular pulse. They achieve this by using the inputs from diagnostics, such as magnetic probes, which verify the magnitude of the magnetic field around the outside of the plasma. Simultaneously, EFIT++ uses the input of the magnetic configuration and solves the Grad Shafranov equation, which is particular form of the force balance equation,

$$\mathbf{J} \times \mathbf{B} = \nabla P \quad (2.5.4)$$

where  $J$  is the current density,  $B$  is the magnetic field and  $\nabla P$  is the pressure gradient. This describes how the magnetic fields exert a pressure on the plasma, which balances with plasma pressure. The magnetic field is then parametrized in terms of the magnetic flux surfaces  $\psi(R,Z)$ , giving the non linear partial differential equation that EFIT++ solves,

$$R \frac{\partial}{\partial R} \left( \frac{1}{R} \frac{\partial \psi}{\partial R} \right) + \frac{\partial^2 \psi}{\partial Z^2} = -\mu_0 R^2 \frac{\partial p(\psi)}{\partial \psi} - \mu_0^2 f(\psi) \frac{\partial f(\psi)}{\partial \psi} \quad (2.5.5)$$

where  $p(\psi)$  is the pressure,  $f(\psi) = RB_\phi$ . Non linear PDEs can't be solved analytically, therefore EFIT++ takes experimental data to work out the equilibrium.

### 2.5.1 Outputs from EFIT++

Fig.2.4 (left) shows a typical slice through the poloidal plane; this is a contour plot of the  $q$  profile for MAST which is generated by EFIT. The plasma boundary is visible, and this particular shot was run in a double null configuration, which can be seen as two x points on the pink line surrounding the plasma. Fig.2.4 (right) shows the contours of the poloidal flux function. The region of greatest poloidal flux in white is caused by the poloidal field coils. In Fig.2.5, input polarization angle from MSE (red) is shown, along with the 'predicted' MSE fit from EFIT++ (black). EFIT++ can be run with just magnetic constraints, but as there is no local constraint for the center of the plasma, there are multiple possible equilibrium solutions. The fit is then said to be ill posed; we are trying to constrain and fit to more data than is available. This is why local measurements from diagnostics are so important. The robustness of the plasma equilibrium proposed by EFIT++ heavily depends on input constraints; the greater the amount of diagnostic data input, the better the fit produced.

### 2.5.2 Magnetic Field Reconstruction

Using the poloidal flux functions output from EFIT++, we can reconstruct the magnetic field for a particular MAST shot. One subtlety to this is that the basis vectors chosen for the flux co-ordinates  $(\nabla\psi, \nabla\theta, \nabla\phi)$  do not form an orthogonal basis set, but this system is chosen as it is much easier to define the magnetic field in terms of flux functions rather than in the machine co-ordinates  $(R,Z,\phi)$ . The contravariant magnetic field components are derived in [12],

$$B^\psi = 0 \quad (2.5.6)$$

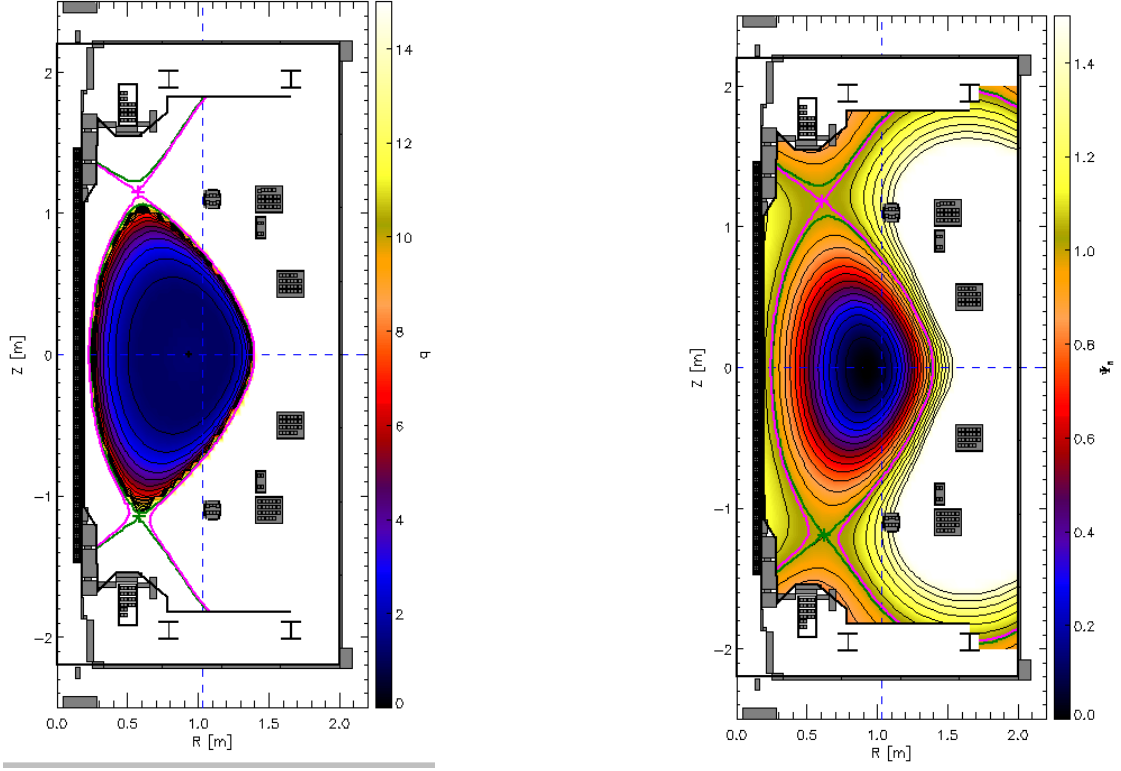


Figure 2.4: **Left:**  $q$  profile across poloidal plane. **Right:** Poloidal magnetic flux across poloidal plane.

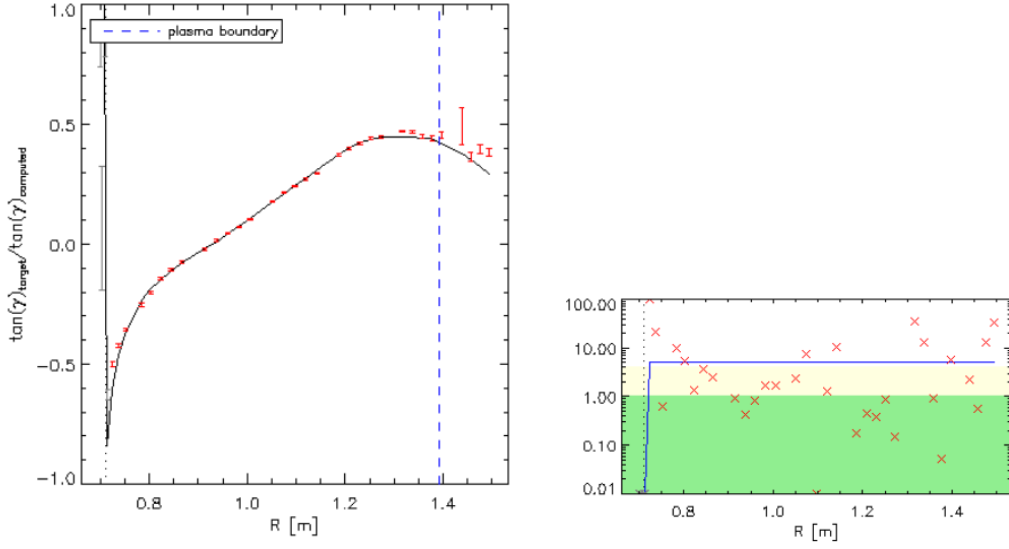


Figure 2.5: **Left:** MSE data (red) with fit from EFIT++ (black). **Right:** Minimized  $\chi^2$  residuals from EFIT++.

$$B^\theta = |\nabla\psi||\nabla\theta| \left[ (Z - Z_0) \frac{\partial\psi}{\partial Z} + (R - R_0) \frac{\partial\psi}{\partial R} \right] \quad (2.5.7)$$



$$B^\phi = \begin{cases} \mu_0 R f(\psi), & 0 \leq \psi \leq 1 \\ B^\phi(R_{\text{ref}}) R_{\text{ref}}, & \psi > 1 \end{cases}$$

where  $f_\psi$  is the current flux function  $B_{vac}$  is the vacuum magnetic field (ie. B field outside of the plasma),  $(R_0, Z_0)$  co-ordinates define the center of the magnetic axis. Then the total magnetic field is,

$$|B| = \sqrt{B_\theta B^\theta + B_\phi^2} \quad (2.5.8)$$

$B_\theta$  and  $B^\theta$  are the contravariant and covariant components of the poloidal magnetic field respectively. Due to toroidal symmetry  $B_\phi = B^\phi$ . An example of magnetic field reconstruction is shown in Fig.2.6.

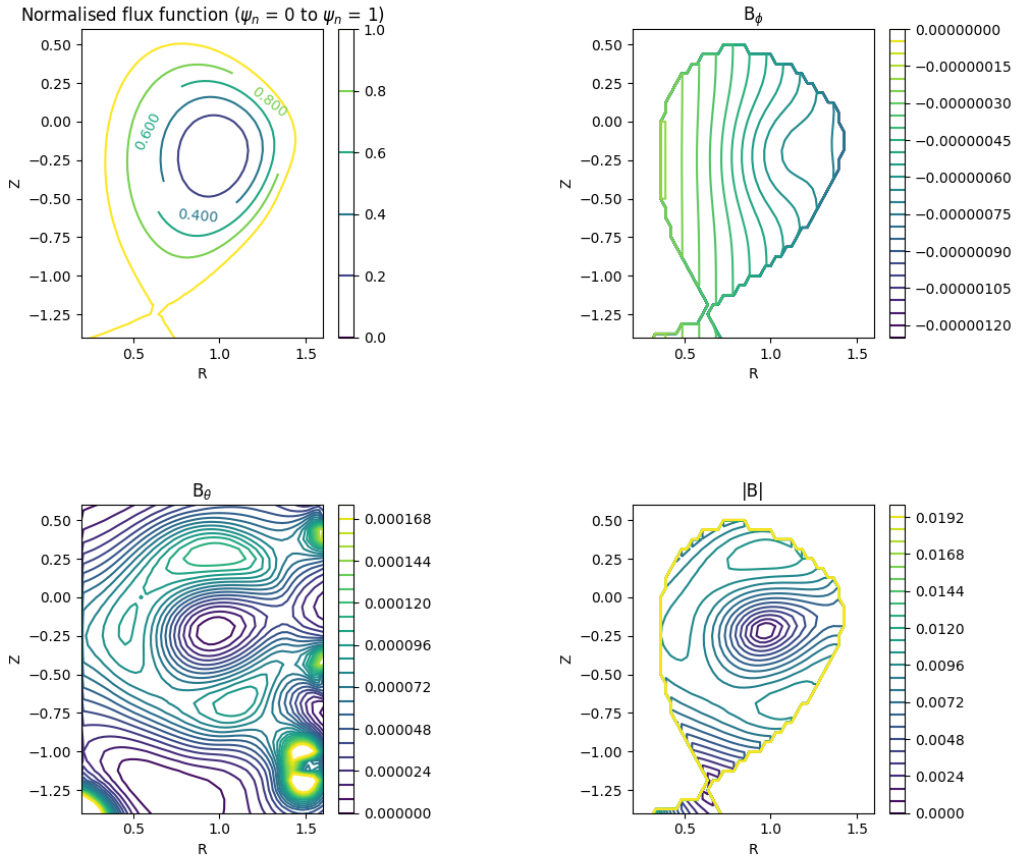


Figure 2.6: Clockwise from top left: Normalised flux function showing last closed flux surface (LCFS), Toroidal B field component, total poloidal B field and the total magnetic field B.

From Fig.2.6, we can infer that this shot was run in single null configuration as only one x-point is present and that the toroidal field falls off as  $1/R$  as expected. Very tight contours in  $B_\theta$  at  $R = 1.5\text{m}$  shows the poloidal field coils.

## 2.6 Current and Future Work

Currently, my work is exploring how MSE data is used as a constraint for EFIT++ and how to improve plasma equilibrium fits. To further this, we will investigate using perturbations to synthetic current density data to see what the variation is in polarization angle. This would give us more insight into interpretation of measurements. Finally, over the next few weeks we will be focusing on installing and calibrating the MSE system on MAST-U.

# Bibliography

- [1] J. Wesson, *The Science of JET*, European Fusion Development Agreement, (2000).
- [2] R. D. Hazeltine & J. D. Meiss, *Plasma Confinement*, Dover Publications Inc., New York, Dover Edition, (2003).
- [3] H. S. Bosch, and G. M. Hale, *Improved formulas for fusion cross-sections and thermal reactivities.*, Nuclear fusion **32**(4) (1992), 611.
- [4] J. Ongena, et al., *Magnetic-Confinement Fusion*, Nature Physics, **12**(5), (2016), 398-410.
- [5] A. Kirk, *Mast Upgrade: Status and Plans*, Spherical Tokamak Workshop, Princeton, USA (2015).
- [6] L. Fernandez-Menchero, S. Henderson and H. Summers, *PUBL4: Neutral Beam Emission: The Motional Stark Effect*, ADAS-EU, (2012).
- [7] H. Yuh, *The Motional Stark Effect diagnostic on Alcator C-Mod*, Massachusetts Institute of Technology Thesis, (2005).
- [8] B. H. Bransden and C. J. Joachain, *Quantum Mechanics*, Second Edition, Pearson Education Ltd, London, (2000), 560-561.
- [9] D. Wreblewski, et al., *Motional Stark Effect polarimetry for a current profile diagnostic in DIII-D*, Rev. Sci. Instrum., **61**(11), (1990), 3552-3556.
- [10] A. Thorman, et al., *A photoelastic modulator based motional stark effect polarimeter for ITER that is insensitive to polarized broadband background reflections*, Rev. Sci. Instrum., **87**(7), (2016), 073504.
- [11] T. Oakberg and B. Wang, *Light Intensity Modulation using a PEM*, Hinds Instruments Application Note, Hinds Instruments, (2013)
- [12] H. Meyer, *The MAST magnetic field*, Culham Center for Fusion Energy, (2001).